CrystEngComm

Accepted Manuscript

ROYAL SOCIETY OF CHEMISTRY

www.rsc.org/crystengcomm

CrystEngComm

RSC Publishing

ARTICLE

Graphene nanosheets encapsulated α-MoO_3 nanoribbons with ultrahigh lithium ion storage properties

Cite this: DOI: 10.1039/x0xx00000x

Received 00th December 2013,
Accepted 00th December 2013

DOI: 10.1039/x0xx00000x

www.rsc.org/

Pei-Jie Lu [a, b], Ming Lei [c], Jun Liu * [a, b]

A facile and effective way has been reported to synthesize of graphene-encapsulated α-MoO_3 nanoribbons by self-assembly between negatively charged graphene oxide and positively charged MoO_3 nanoribbons. Compared to those structures of MoO_3 nanobelts grown on graphene or other hybrids of MoO_3 composited with carbon or non-carbon, this unique hybrid architecture of graphene-encapsulated MoO_3 nanoribbons exhibits not only a high specific capacity (up to 823 mAh•g^{-1} after 70 cycles at 200mA•g^{-1}), but also an excellent cycling performance (with more than 754 mAh•g^{-1} after 200 cycles at 1000mA•g^{-1}) as well as a greatly-enhanced high-rate capability (displaying a high discharge capacity of 710 mAh•g^{-1} after 30 cycles at 3000 mA•g^{-1}), thus holding a great potential as an anode material for lithium ion batteries.

1 Introduction

Looking forward to the energy future of humanity, renewable energy will definitely be the most sustainable way to solve many social and environmental problems. How to store the variable renewable energy in an efficient and cheap way would be a great challenge. The most promising energy storage systems should combine the features of relatively high energy density, good power capability, environmental friendliness, and low cost. Lithium ion batteries (LIBs) are considered among the most practical and effective technologies for electrochemical energy storage.[1, 2] LIBs can be widely used in electric vehicles, multifunctional electric devices, communication equipment, and renewable energy integration.[3, 4] Therefore, developing LIBs with high energy density, power density, and excellent cycling performance becomes critical. Numerous efforts have been devoted to develop the new electrode materials to meet these demands of LIBs.[2, 3, 5] Electrochemically active transition metal oxides (M_xO_y), such as Fe_2O_3 ,[6, 7] Fe_3O_4 ,[8] SnO_2 ,[9] Co_3O_4,[10-12] and TiO_2 [13, 14] may be used as promising candidates for anode materials in the future owing to their high theoretical capacity and natural abundance. Among the metal oxide, molybdenum trioxide (MoO_3) has recently received much attention as an electrode material for LIBs owing to its good chemical stability and high charge storage capability. MoO_3 is a well-known Li^+ insertion compound and has been investigated during the early years of lithium battery research.[15-17] As an anode material, MoO_3 not only has a superior theoretical specific capacity of nearly 1111mAh•g^{-1},[18] which is nearly three times than that of graphite (372mAh•g^{-1}) [19], but also has a very stable layered structure (as show in scheme 2a). [20, 21] This layered structure is able to act as a temporary host for intercalated Li^+.[22] However, the poor conductivity and poor kinetics of Li^+ diffusion in bulk layered MoO_3 limits its electrochemical performances.[23]

One way to enhance the kinetics for lithium storage in MoO_3 is to prepare nanostructured MoO_3, which can enlarge the surface area of active material and lessen the diffusion dimension of charges. [24-26] Another way is to synthesize MoO_3-carbon composite, which not only prevents the exfoliation of active material from current collector but also improves the conductivity of MoO_3.[18] In this regard, Sn-Co-CNT@ CNT,[27] Si/graphene,[28] Si@CNT,[29] SnO_2/graphene,[30] $LiFePO_4$@ CNT[31], TiO_2/graphene,[32] Graphene/CNT@Porous Carbon-S[33] and Co_3O_4/graphene,[34] hybrids or composites, in which metals or metal oxides are distributed onto the surface of graphene or between the graphene layers, have been fabricated by restacking CNT or graphene sheets in the presence of guest nanoparticles or corresponding organometallic precursors. In particular, graphene, a new two-dimensional carbon material, exhibits superior electrical conductivity, large surface area, structural flexibility, and chemical stability, is greatly pursued by chemists and materials scientists since it was proposed.[35, 36] Therefore, graphene is regarded as a promising substitute for graphite to prepare high performance MoO_3 - carbon composite. MoO_3 nanobelts grown on reduced graphene oxide or graphene have been reported by hydrothermal methods,[37, 38] however, as far as we known, the graphene-encapsulated MoO_3 nanoribbon has not been reported. Although these reported MoO_3 nanomaterials or MoO_3-graphene composites have shown improved performances, achieving MoO_3 with good rate performances and stable cycling properties still remains a great challenge until now.

In this work, we initially come up with the idea that the α-MoO_3 nanoribbon can be modified by APS to achieve the fabrication of graphene-encapsulated α-MoO_3 nanoribbon by

self-assembly between negatively charged graphene oxide and positively charged MoO_3 nanoribbons. The strategy mainly includes three steps. Firstly, APS were used to modify the α-MoO_3 nanoribbon so as to make the α-MoO_3 nanoribbon positively charged. Secondly, we mix the positively charged MoO_3 nanoribbons and the negatively charged graphene oxide. Last, graphene oxide-encapsulated α-MoO_3 nanoribbon by the mutual electrostatic interactions of the two species is followed by chemical reduction in H_2/Ar atmosphere and high temperature pyrolysis of GO (as shown in scheme 1a, b). As a result, we achieved the fabrication of graphene-encapsulated α-MoO_3 nanoribbon by self-coassembly between negatively charged graphene oxide and positively charged MoO_3 nanoribbons. The resulting α-MoO_3@GNS nanocomposite possesses flexible and ultrathin graphene shells that effectively enwrap the α-MoO_3 nanoribbons. Compared to those structures of MoO_3 nanobelts grown on reduced graphene oxide or graphene, this unique hybrid architecture of graphene-encapsulated MoO_3 nanoribbon can take several advantages: 1) suppress the aggregation of α-MoO_3 nanoribbons, 2) accommodate the volume change during the cycle processes, 3) greatly improve the transportation efficiency of current carriers, 4) maintain a high electrical conductivity of the overall electrode (as shown in scheme 1c). Most importantly, the α-MoO_3@GNS exhibits not only a high specific capacitance (up to 823 mAh•g^{-1} after 70 cycles at 200mA•g^{-1}), but also an excellent cycling performance (with more than 754 mAh•g^{-1} after 200 cycles at 1000mA•g^{-1}) as well as a greatly-enhanced high-rate capability (displaying a high discharge capacity of 710 mAh•g^{-1} after 30 cycles at 3000mA•g^{-1}), thus holding a great potential as an anode material for lithium ion batteries.

2 Experimental section

2.1 Preparation of the α-MoO_3 @ Graphene nanohybrids

Synthesis of materials: All chemicals were of analytical purity and were used as received without further purification.

GO Synthesis: GO solution was made using a modified Hummers'method.[39-41] Briefly, 1 g of raw graphite powder (SP-1), 0.5 g of $K_2S_2O_8$, and 0.5 g of P_2O_5 were stirred in 3 mL of H_2SO_4 at 80℃ for 4.5 h and copiously washed and dried in air overnight. Then 3 g of $KMnO_4$ was slowly added to the graphite powder solution with 23 mL of H_2SO_4 at 0℃. After vigorous stirring at 36℃ for 2 h, 46 mL of deionized water was added at 0℃ and the solution was stirred at 36℃ for additional 2 h. The oxidation step was completed by the addition of 140 mL of DI water and 2.5 mL of H_2O_2 solution (35%). The GO solution (brown color) was washed, and filtrated with 250 mL of HCl (10%). Before complete drying, the GO was dispersed in DI water (10 mg•mL^{-1}) and dialyzed for 2 weeks, from which pH values attained ≈ 6 to 7.

α-MoO_3 nanoribbons synthesis: The α-MoO_3 nanoribbons were synthesized by hydrothermal treatment of a peroxomolybdic acid solution. The peroxomolybdic acid precursor solution was prepared as follows: 80 mL of 30 wt % H_2O_2 aqueous solutions were slowly added to a round bottle flask containing of 9.6 g of Mo metal powder in an icy water bath with violent magnetic stirring. A transparent yellow solution was obtained, and it was further diluted to 0.10 mol/L. In a typical synthesis of α-MoO_3 nanoribbon, 30 mL of precursor solution was sealed in a 50 mL autoclave and hydrothermally treated at 180 ℃ for 24 h.[42] A white colloidal suspension was obtained, and then, the α-MoO_3 paper was prepared by vacuum filtration and washed thoroughly with distilled water. After dried, the α-MoO_3 paper was grounded for use.

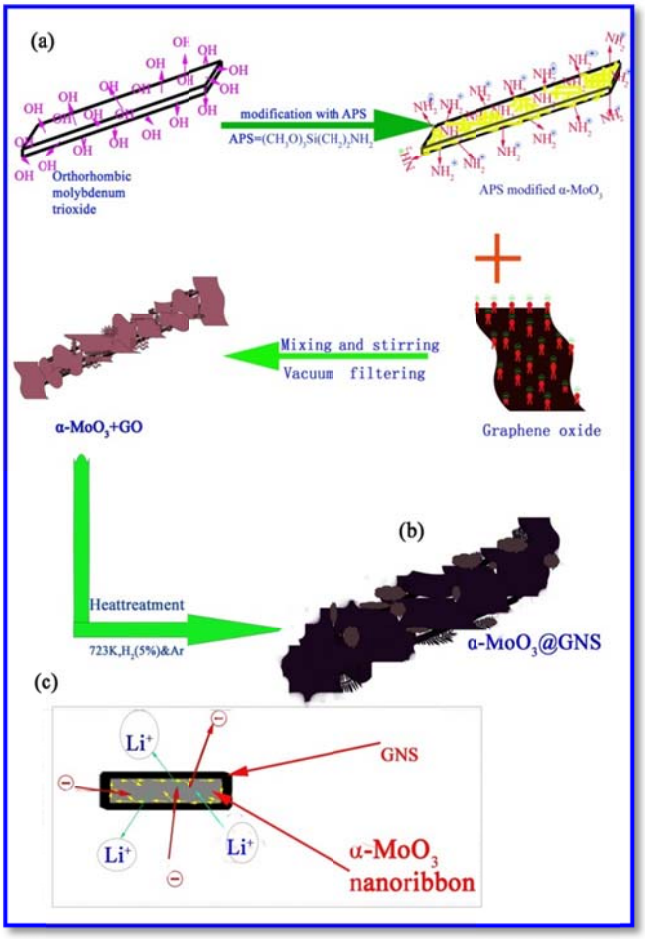

Schime.1 Schematic illustration of **(a)** formation process of graphene-encapsulated α-MoO_3 nanoribbon nanocomposite, including: 1)modification of the α-MoO_3 nanoribbon by grafting aminopropyltrimethoxysilane (APS) to render the oxide surface positively charged; 2) hybrid assembly between positively charged α-MoO_3 nanoribbon and negatively charged graphene oxide by electrostatic interactions; and 3) chemical reduction of α-MoO_3 nanoribbon,**(b)** sketched morphological features, and **(c)** proposed cross-sectional Li^+/e^- transfer mechanism in graphene-encapsulated α-MoO_3 nanocomposite.

Assembly of α-MoO_3 nanoribbons @GO hybrids and Heat-Treatment: MoO_3 nanorribbons were firstly modified by surface grafting of aminopropyltrimeth-oxysilane (APS) to render the oxide surface positively charged. More specificly, 0.432g α-MoO_3 were dropped into 30ml aqueous solution containing 2% wt APS with a vigorous stirring for 30min , meanwhile 10mL GO solution (10mg/mL) were added into the former with vigorous stirring for another 30 minitues , after that the mixture were vacuum filtration. The as-formed product was subsequently treated at 450 ℃ (ramp rate: 10 ℃ min^{-1}) in a atmosphere of 800 sccm (standard cubic centimeter) gas mixture (95% Ar and 5% H_2) for 20 minutes. Once the annealing time was out, it was suddenly cooled by taking off

the lid of the furnace.[43, 44] Finally, the black-coloured product of MoO_3@GNS was collected for further characterizations.

The process used to prepare the anode is described below. The Li/ MoO_3@GNS coin cells are assembled in a glove box (Mbraun, Germany) using metallic lithium as anode, polypropylene separator, and 1M solution of $LiPF_6$ in ethylene carbonate/dimethyl carbonate (EC/DMC) (1:1, v/v) as electrolyte. The galvanostatic charge/discharge performances of the electrodes were evaluated at room temperature using a Land Battery Tester (Land CT 2001A, Wuhan, China) within the voltage range of 0.01 V-3V (vs. Li/Li^+). The loading of the α-MoO_3@GNS anode material for coin cell test is about 1-2mg. Cyclic voltammetry (CV) was tested on an electrochemical workstation（CHI660C, China）at a scan rate of 0.05 $mV•s^{-1}$ in the voltage range of 0.01-3V (vs. Li/Li^+). The electrochemical impedance spectrometry (EIS) was performed on a ZAHNER-IM6ex electrochemical workstation (ZAHNER Co.Germany) in the frequency range of 100 kHz to 10 mHz on a cell in as-assembled condition.

3 Result and discussion

3.1 Structural characterization

A combined Differential Scanning Calorimetry (DSC) and Thermogravimetric Analysis (TGA) instrument (SDT,Q600) was used to study the evolution of the precursor in air at a heating rate of 5 ℃ $•min^{-1}$. The phases of the as-prepared products were studied by X-ray power diffraction (XRD, Rigaku D/max 2500 XRD with Cu-Kα radiation, λ=1.54178 Å). The morphologies and sizes of the as-prepared products were characterized by scanning electron microscopy (SEM, FEI Nova Nano SEM 230) and transmission electron microscopy (TEM, JEOLJEM-2100F).

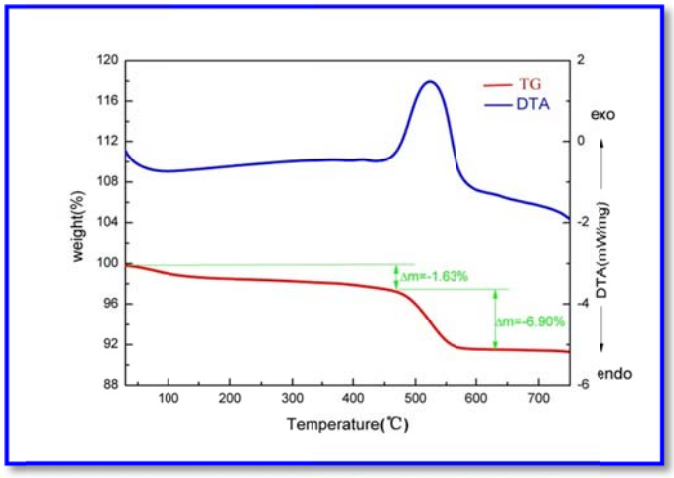

Fig. 1 TG and DTA data for the nanocomposites of α-MoO_3 nanoribbon@GNS.

Fig. 1 shows the TG and DTA results of the composite of α-MoO_3 nanoribbons @GNS under flowing air with a temperature ramping rate of 5℃ /min. The slow weight-loss between 30℃ and 450 ℃ shown in Fig. 1 can be attributed to the loss of physically and chemically bonded water and partial decomposition of GO in the composite. The significant weight loss shown on the TG curve and a corresponding exothermal peak on the DTA curve between 450 ℃and 550 ℃ are related to the combustion of graphene nanosheets (GNS), the weight of which reached 6.90% in the nanohybrids.

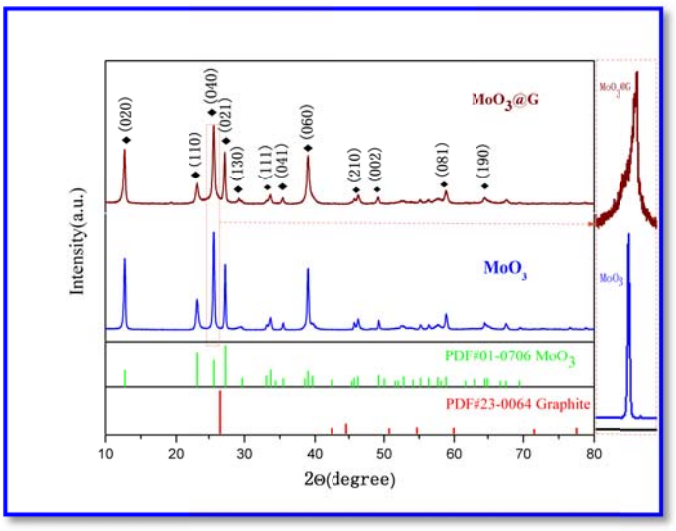

Fig. 2 XRD patterns for the sample fabricated at 450℃ under 800 sccm gas mixtures (95%Ar and 5% H_2).

XRD measurement was used to study the phase and lattice modification of the α-MoO_3 nanoribbons@GNS. The diffraction peaks of the XRD pattern for the sample can be readily indexed to be orthorhombic MoO_3 i,e. α-MoO_3, whose lattice parameters is a =0.3966 nm, b = 1.388 nm, and c =0.3703 nm, and of which space group is P*bnm* (Joint Committee on Powder Diffraction Standards, JCPDS No.05-0507).[42] No peaks of any other molybdenum oxide phases were detected, indicating the high purity of the α-MoO_3 nanoribbons. For the α-MoO_3 nanoribbons, the intensities of (020), (040) and (060) peaks are stronger than those of the bulk MoO_3 which indicates the anisotropic growth of the nanostructure as well as the preferred orientation of the nanoribbons. From partial enlarged detail of the XRD pattern, we can see that the stronger intensity peak (040) at 2θ≈25.879° of pure α-MoO_3 nanoribbon become a broader one when GNS combined with MoO_3 nanoribbon. The characteristic (002) diffraction peak of the graphene nanosheets appear at about 22 - 26° as well. The defect and few layers deteriorate the integrity of graphite crystal structure which make GNS a amorphous-like material, so the intensity peak (002) become a broader one, as shown in the Supporting information Fig. S1. Due to the superposition of the two peaks, the stronger intensity peak (040) at 2θ≈25.879° of α-MoO_3 nanoribbon@GNS becomes a broader one. Meanwhile, from partial enlarged detail of the XRD pattern, we can't see that the characteristic diffraction peak of the graphene oxides (GO) between 10 - 15° in XRD pattern of the annealed sample. Therefore, it can be conformed that the GO had been reduced to the ultrathin defective GNS after annealing treatment. The similar experiment is also reported by Müllen and Zhang.[40, 45, 46]

Raman spectroscopy was used to further investigate the structural features of MoO_3@GNS and the carbon matrix GNS in the MoO_3@GNS composite (Fig. 3a). The peak at ~1350 cm^{-1} (D band) is assigned to defects and disorder in the GNS. The distinctive peak at ~1580 cm^{-1} (G band) is related to the

coplanar vibration of sp^2-bonded carbon atoms in GNS. According to the Raman spectra comparison between GO and GNS (shown in Fig. S2), the Fig. 3a indicates that our sample is the MoO_3@GNS composite, not MoO_3@GO composite, since the intensity of D peak is higher than that of G peak. Moreover, the peak intensity ratio between the 1350 and 1580 cm^{-1} peaks (I_D/I_G) generally provides a useful index about the degree of crystallinity of various carbon materials, that is, the smaller the I_D/I_G ratio, the higher the degree of ordering in the carbon material.[47] The intensity ratio I_D/I_G of ≈1.2 indicates the size of the graphitic carbon (L_a) is about 5.3 nm according to the empirical equation $L_a = 4.4\ I_D/I_G$ (nm).[41] These results indicate that the carbon matrix is partially graphitized, which could benefit the electron transportation from/to the poorly conducting MoO_3. The 2D band (2708 cm^{-1}) is the most prominent feature in the Raman spectrum of GNS in the MoO_3@GNS composite, and its position and shape are sensitive to the number of layers of graphene. The single, symmetrical 2D band exhibited at 2708 cm^{-1} corresponds to the graphene with a few layers. Fig. 3a showed the Raman spectra of the MoO_3@GNS composite. The Mo-O stretching (ν) and bending (δ) vibrations usually appear in the 1000-600 cm^{-1} and 600-150 cm^{-1} range, respectively. The Raman spectra of the MoO_3@GNS composite showed the characteristic Raman bands of MoO_3 at 993 (A_g , ν_{as} M=O stretch), 817 (A_g , ν_s M=O stretch), 665 (B_{2g}, B_{3g} , ν_{as} O-M-O stretch), 473 (A_g ,ν_{as} O-M-O stretch and bend), 380 (B_{1g} , δ O-M-O scissor), 376 (B_{1g}), 366 (A_{1g} , δ O-M-O scissor), 334 (A_g, B_{1g} , δ O-M-O bend), 293 (B_{3g} , δ O=M=O wagging), 285 (B_{2g} , δ O=M=O wagging), 247 (B_{3g} , τ O=Mo=O twist), 216 (A_g , rotational rigid MoO_4 chain mode, R_c), 197 (B_{2g} , τ O=Mo=O twist), 159 (A_g/B_{1g} , translational rigid MoO_4 chain mode,T_b), 129 (B_{3g} , translational rigid MoO_4 chain mode, Tc), 116(B_{2g} , translational rigid MoO_4 chain mode, Tc), 100 (B_{2g} ,translational rigid MoO_4 chain mode, T_a) and 89 cm^{-1} (A_g ,translational rigid MoO_4 chain mode, T_a). The observed bands are assigned according to the single crystal study of Py etal.[48] The Mo=O bond distances along the *a*- and *b*-axes (167 and 173 pm) are shorter than the Mo-O bond distance along the *c* axis (195 pm). The high stretching frequency at 993 and 817 cm^{-1} can be assigned to the stretching vibration of the terminal Mo=O bonds along the *a*- and *b*-axes.[49] The high intensity of 993 and 817 cm^{-1} bands may indicate that the high oxygen vacancy concentration in MoO_3@GNS composite,[48] which may result from the sample annealing in an atmosphere of 800 sccm gas mixtures (95% Ar and 5% H_2).

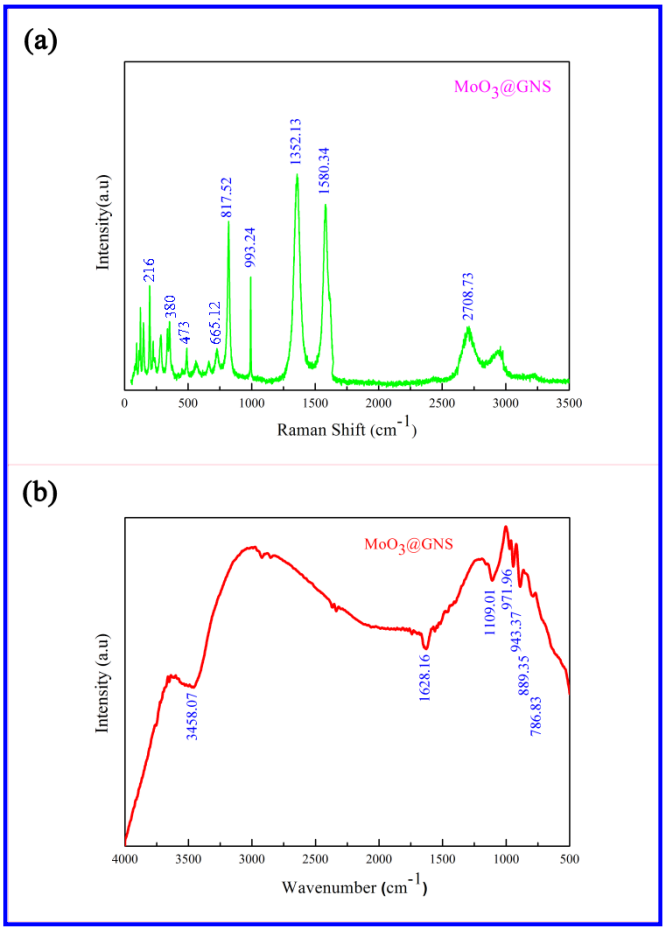

Fig. 3 (a) Raman spectra of MoO_3@GNS, (b) FT-IR spectra of MoO_3@GNS composite.

The FT-IR spectra in Figure 3(b) support a consistent conclusion. The stretching mode of Mo-terminal oxygen is located at 991 cm^{-1}. The absorption bands at 867 and 555 cm^{-1} are assigned to stretching vibrations of the O(3) and O(2) atoms linked to two or three molybdenum atoms, respectively. The absorption bands at 1628 cm^{-1} was caused by stretching vibrations of sp^2 hybridized carbons C=C in graphene. From 3000 to 3700 cm^{-1}, there was a broad absorption peak which came from a small quantity of –OH. The intensity of absorption peak at 1720 cm^{-1} attributes to the stretching vibrations of C=O in –COOH,[41] the intensity of which are very weak because the GO was reduced sufficiently by H_2 during the heat treatment. The FT-IR spectra of the GO and GNS product was also shown Fig. S3.

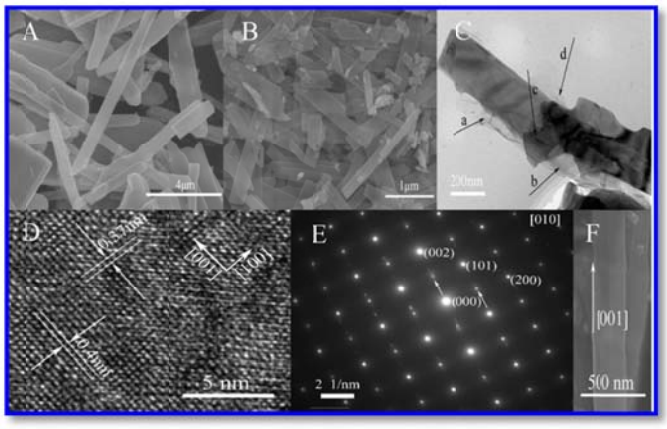

Fig. 4 (A,F) SEM image of the α-MoO_3 nanoribbon (B) SEM image of the α-MoO_3@GNS nanocomposite and (C) TEM images of the α-MoO_3 @GNS composite; (D,E) HRTEM and SAED of the MoO_3@GNS composite.

The morphology and structure of the α-MoO_3@GNS nanocomposite were characterized by SEM and TEM. Figure 4A and B present the top-view SEM images of pure α-MoO_3 nanoribbons and α-MoO_3@GNS composite, respectively. Uniform α-MoO_3 nanoribbons with width of 300-600 nm and lengths of 4-10 μm can be observed clearly from image A. However, the thicknesses of the nanoribbons are hard to determine from the SEM images. From Figure 4B, we can found that the α-MoO_3 nanoribbons were not that uniform and smooth comparing with image A, which resulted from the GNS adhering to α-MoO_3 nanoribbons. To further understand the morphology and structure characteristics of α-MoO_3@GNS composite, TEM and corresponding selected area electron diffraction (SAED) and HRTEM pattern are shown in panels C, D and E of Figure 4, respectively. Figure 4C shows a typical TEM image which further confirms special structure of graphene nanosheets encapsulated α-MoO_3 nanoribbons, and the overall belt-like morphology of as-prepared products, the bottom (a), side (b, d), and upper side(c) of α-MoO_3 nanoribbons all were wrapped up by the ultrathin graphene which can enormously increase the electric conductivity of the nanocomposites and buffer the strain from the change in volume of α-MoO_3 nanoribbons during the cycling process. Moreover, the TEM image in Figure 4C reveals that the α-MoO_3 nanoribbon is firmly attached to the GNS even after long time ultrasonic treatment, suggesting strong interaction between α-MoO_3 nanoribbon and GNS, which could contribute to effective electrostatic interaction caused by APS between the two materials. This special structure characteristic can well-explain the perfect cycling performance and rate performance illustrated in Figure 6. From the contrast along the width of the nanoribbons (refer to Figure 4F), it is obvious that the observed nanoribbons are actually composed of two parallel and closely stacked single nanoribbons. It is of interest to note that, although the observed nanoribbons are composed of two single nanoribbons, only one set of electron diffraction spots can be detected, indicating that two parallel nanoribbons have identical crystallographic orientation. The most possible reason for this phenomenon is "oriented attachment". [42] The SAED pattern shown in Figure 4E can be attributed to the [010] zone axis of orthorhombic α-MoO_3. It should be mentioned that, besides the allowed diffraction spots such as 200* and 002*, some forbidden diffraction spots can also be observable (such as 100* and 001* indicated by white arrows), which can be explained as the double diffraction caused by the dynamic scattering of the strong electron beam. On comparison of the TEM image and its corresponding SAED pattern, it is confirmed that the α-MoO_3 nanoribbons grow along the [001] direction and along the (010) plane (as shown in scheme 2a, b). Two sets of crystal lattice fringes, corresponding to the {100} (0.40 nm) and {001} (0.37nm) atomic spacings (as shown in scheme 2c, d), can be clearly distinguished in the top-view high-resolution HRTEM image of the α-MoO_3 (Figure 4D).

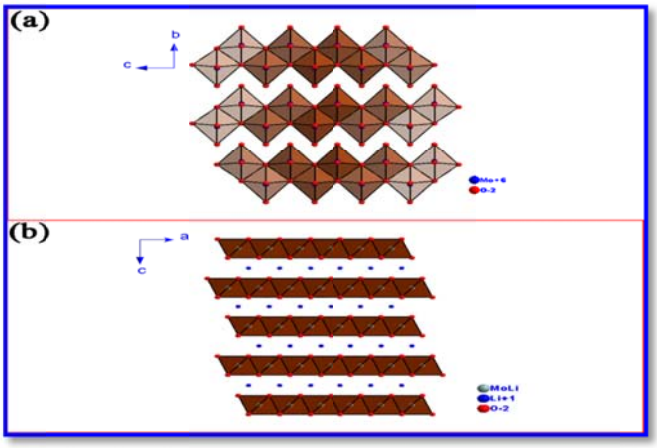

Scheme 2. Schematic of stable layered α-MoO_3 structures and lithiated MoO_3.

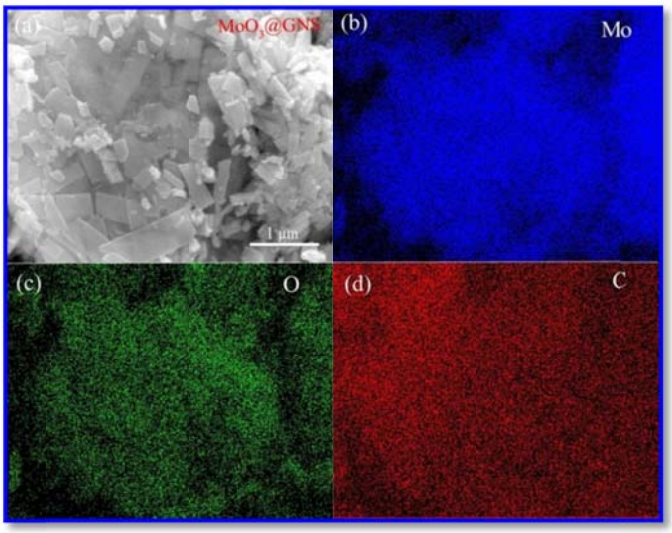

Fig. 5 SEM image and the corresponding elemental mapping of Mo, O and C in the graphene nanosheets encapsulated α-MoO_3 nanoribbons nanostructures.

Energy dispersive spectroscopy (EDS) reveals that the nanocomposite of nanoribbon α-MoO_3@GNS consists of the elements Mo, O and C (shown in Figure 5), which is consistent with the XRD, Raman and TEM results (Figures 2, 3 and 4). Moreover, from the SEM image (Fig.5a) and the corresponding elemental mapping of C (Fig.5d), we can see that the nanoribbon α-MoO_3 is uniformly wrapped up by the GNS which illustrates we have successfully achieved the preparation of graphene nanosheets encapsulated α-MoO_3 nanoribbons.

3.2 Electrochemical performance

To address the effect of nanocoating layer (GNS) on the electrochemical performance of the α-MoO_3 nanoribbon, we have studied the electrochemical performance of α-MoO_3@GNS nanocomposites and pure α-MoO_3 nanoribbon on the same time.

Fig. 6a indicates the Li^+ insertion/extraction capacities and the coulombic efficiency of the α-MoO_3@GNS and the α-MoO_3 nanoribbon. From the chart we can see that under a current density of 200 mA•g^{-1} between the voltage limits of 0.01 and 3.0V (vs. Li^+/Li), the α-MoO_3@GNS anode has a high specific capacity and a perfect cycle performance. The initial discharge capacity reached 1321 mAh•g^{-1} and the second discharge capacity reached 953 mAh•g^{-1}, the large capacity loss in the first two cycles is mainly attributed to the irreversible intercalation of Li^+ ions into the crystal lattice which results in the structural change of MoO_3 and the formation of Li_2O. The structural change of MoO_3 at the end of the first recharge can't be fully recovered after the initial discharge which plays an important role in the large capacity loss. The similar results are reported by T.Tsumura, Minoru Inaba, etc.[50, 51] Meanwhile some other irreversible processes such as inevitable formation of solid-electrolyte interface (SEI) layer also may result in the capacity loss as well, which are common for most interstitial-free transitional metal oxides anodes. The specific discharge and charge capacity of α-MoO_3@GNS anodes experienced a sluggish increase firstly, and then almostly sustain the same level and even after 70 cycles, there was still 833 mAh•g^{-1} remained to the nanoribbon α-MoO_3@GNS anodes, which is 2.2 times more than the theoretical capacity of graphite (372 mAh•g^{-1}). The coulombic efficiency increases at the initial few cycles and after several conditioning cycles, the coulombic efficiency of the coin cell increased to higher than 99% (Figure 2b, c), indicating good reversibility of the interaction and extraction of Li^+ in the nanocomposite.

To further understand the cyclic performance of nanoribbon α-MoO_3@GNS electrodes, the voltage-capacity curves of the nanoribbon α-MoO_3@GNS sample in the 1st, 20th, 30th, 40th, 60th and 70th cycles at 0.2C (200mA•g^{-1}) discharge rate are shown in Fig. 6b. The charge and discharge platform were 1.3V and 0.6V, respectively. The discharge capacity of 1st, 20th, 40th, 60th and 70th cycle are 1321, 984, 980, 900 and 843 mAh•g^{-1}, respectively. From 2nd to 70th, there was only 14.3% attenuation of capacity, which means only a 0.2% capacity decrease per cycle. Moreover, we can see that the discharge plateaus in the 1st are higher and the charge plateaus are lower compared to consequent cycles. This was due to irreversible reactions between Li^+ and GNS and decomposition of the electrolyte solvent, forming a solid electrolyte interphase (SEI) when a current was applied and the SEI film form gradually in the first few cycles. After that, the charge plateaus voltage rises and discharge plateaus voltage decreases synchronously with cycling,

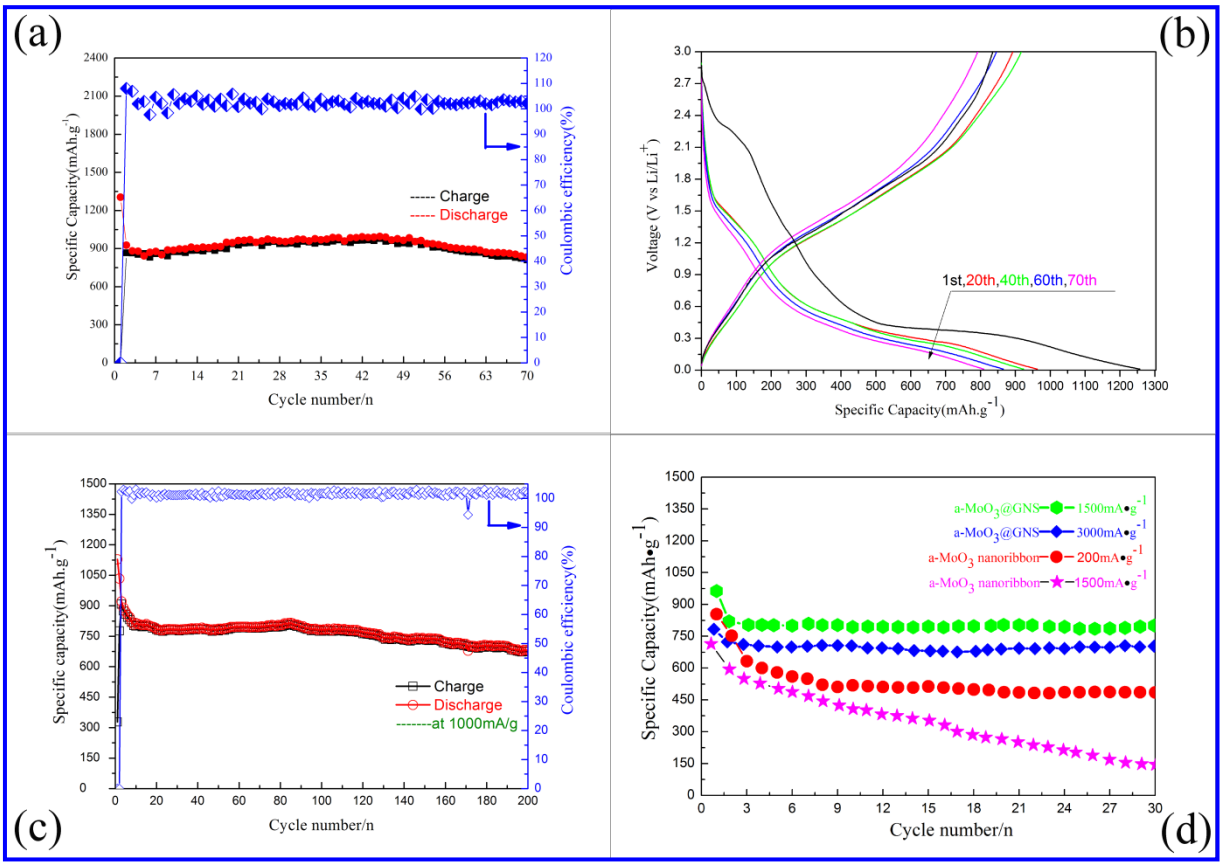

Fig. 6 (a). Cyclic performances of the α-MoO_3@GNS anode at 200 mA•g^{-1}; (b).Charge-discharge curves of different cycles for the **α**-MoO_3@GNS anodes at 200 mA•g^{-1} in the range of 0.01-3V; (c). Cycling performance and Coulombic efficiency of the **α**-MoO_3@GNS anodes in the voltage range of 0.01-3.0 V at a current density of 1000 mA•g^{-1}; (d). Rate performances of the **α**-MoO_3@GNS and the **α**-MoO_3 anodes.

indicating that the reversible capacity decreases gradually. At this time, the second deposition of lithium ions occurs on SEI surface, leading to the increase of SEI thickness and the decrease of reversible capacity. The charge–discharge plateaus of α-MoO_3@GNS are very close with the increase of the cycles, suggesting the reversible capacity of α-MoO_3@GNS decreases slowly which is probably due to its small electrode polarization. The charge and discharge capacities of the α-MoO_3@GNS electrode for the 2nd and 70th cycles are 926 mAh•g^{-1} and 843 mAh•g^{-1}, respectively, which illustrate the GNS in the nanocomopsites greatly improve the capacity and cycling properties. The reasons of excellent cycling properties and high capacity are considered as follows: (i) GNS plays a "flexible confinement" function to enwrap α-MoO_3, which can compensate for the volume change of α-MoO_3 and prevent the detachment and agglomeration of pulverized α-MoO_3, thus extending the cycling life of the electrode; (ii) GNS provides a large contact surface for individual dispersion of well-adhered α-MoO_3 and act as an excellent conductive agent to provide a highway for electron transport, improving the accessible capacity; (iii) α-MoO_3 separate GNS and prevent their restacking thus improving the adsorption and immersion of electrolyte on the surface of electroactive material; and (iv) the porosity formed by lateral GNS and α-MoO_3 facilitates ion transportation.

The excellent cycling performance of the α-MoO_3@GNS nanocomposite is presented in Figure 6c. The generally overlapping profiles indicate the good reversibility of the electrochemical processes upon cycling. With a voltage window of 0.01-3.0V and the high charge and discharge current density (1000mA•g^{-1}), the α-MoO_3@GNS nanocomposites retain a remarkable reversible capacity of 754.6 mAh•g^{-1} at the end of the 200th cycle, which corresponds to a capacity fading rate of only 0.1 % per cycle. For the voltage windows (0.01-3.0 V), the Coulombic efficiency remains close to 100 % during the cycling tests, suggesting the excellent reversibility of the electrodes and stable cycling performance.

The most significantly improved property of the α-MoO_3@GNS anode is the excellent rate performance, as shown in Fig. 6d. The α-MoO_3@GNS still displays a reversible capacity of 820 and 710 mAhg^{-1} after 30cycles when the current density increases to 1500 mA•g^{-1} and 3000 mA•g^{-1}, respectively, which are higher than the capacity of 493 mAh•g^{-1} of α-MoO_3 nanoribbon anode after 30 cycles at discharge current of 200 mA•g^{-1}.When the current density increases to 1500 mA•g^{-1}, the capacity of the pure α-MoO_3 nanoribbon electrode experienced a quick loss, from the initial 693 mAhg^{-1} decreasing to 150 mAhg^{-1} only after 30 cycles. The high-rate performances of the α-MoO_3@GNS anode also show obvious improvement compared with the previous α-MoO_3 anode materials.[18, 52, 53] The superior rate performance of the α-MoO_3 can be attributed to the better Li^+ diffusion kinetics in the α-MoO_3 nanoribbon than in the pristine MoO_3 powder. What's more, the GNS wrapping up the α-MoO_3 plays a very important role. Firstly, the ultrathin GNS has a perfect electronic conductivity which enormously improves the conductive ability of the insulating MoO_3. Secondly, the ultrathin GNS wrapped up the MoO_3 nanoribbons which can restrain the volume expansion and even the pulverization of crystal MoO_3 nanoribbons when charging and discharging. The results of electrochemical impedance spectroscopy (EIS in Fig 8) can verify the important role of GNS in improving the conductivity of the nanocomposites. The special structure characteristic as shown in Fig 4-5 can also illustrate these points.[49]

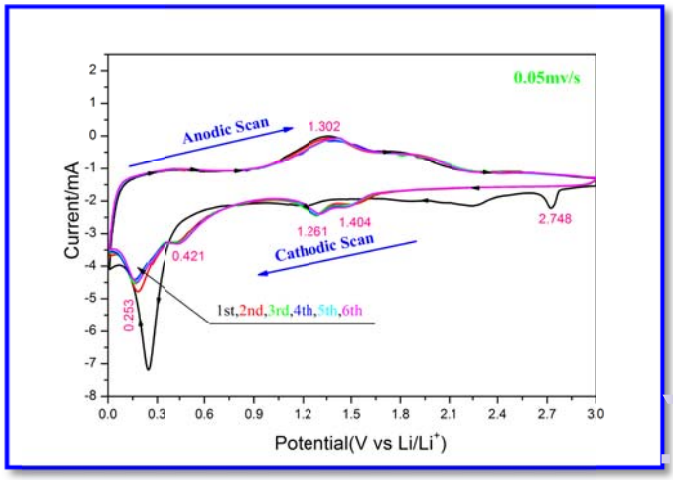

Fig. 7 CV curves of the initial six cycles of the α-MoO_3@GNS anode.

Cyclic voltammetry (CV) experiments were conducted to evaluate the electrochemical performance of α-MoO_3 @GNS at a scanning rate of 0.05 mV•s^{-1} over the voltage range 0.01–3.00V. Fig.7 shows the CV curves for the 1st, 2nd, 3rd, 4th, 5th and 6th cycles of the α-MoO_3 @GNS anodes, which also shows the structural and electrochemical information during the Li^+ insertion/extraction process. In the 1st Li^+ insertion process, four peaks are observed at 2.748, 2.313, 1.235 and 0.27 V. The irreversible reduction peak at ~ 2.748 and 0.27 V in the 1st negative run is mainly attributed to the irreversible intercalation of Li^+ ions into the crystal lattice which results in the structural change of MoO_3 and the formation of Li_2O. The structural change of MoO_3 at the end of the first recharge can't be fully recovered after the initial discharge. The similar results are reported by T.Tsumura, Minoru Inaba, etc.[51, 54] Meanwhile some other irreversible processes lead to the reduction peak as well, such as inevitable formation of solid-electrolyte interface (SEI) layer, which are common for most interstitial-free transitional metal oxides anodes. The irreversible reduction of electrolyte and the formation of a passivating surface film, i.e. the formation of a solid electrolyte interface (SEI) layer, disappeared in the following cycles. The other two peaks in the 1st negative run may be also attributed to the Li^+ insertion process. Then, the voltage plateau decrease slowly to 0.01 V, associated with a conversion reaction of MoO_3 with lithium. In the subsequent processes, all the peaks for the different oxidation–reduction pairs of 0.253/0.563, 1.261/1.312, and 1.404/1.924 V are reversible, due to Li^+ insertion/extraction with different site energies and the phase transition process of Li_xMo alloy and α-MoO_3. The major lithium extraction potential is close to 1.302 V vs. Li/Li^+ reference electrode. The peaks (0.253, 0.421, 1.261, 1.404 V) in the continue cycles may be from Li_xMo alloys in the subsequent steps. The lithiation in MoO_3 is believed to take place in two stages: Stage-I occurs up to a potential of 1.5 V. During this stage, Li intercalates with MoO_3 as follows: [55]

$$MoO_3 + xLi^+ + xe^- \leftrightarrow Li_xMoO_3 \quad (1)$$

The lithium content in this solid solution ranges between 1 and 1.5V, up to a potential of 1.5 V. The high lithium content is accommodated in the interlayer spacing between octahedral Mo−O layers and interlayers. Most of the Li ions intercalated at the potentials (1.261 and 1.404 V) can subsequently be extracted from the material leading to reversibility of the

reaction. Lithium ion intercalation during stage-II corresponds to potentials below 0.7 V and occurs by the following mechanism[54]:

$$Li_xMoO_3 + xLi+ + xe^- \rightarrow Mo + 3Li_2O \quad (2)$$

In the lower voltage range, lithium reacts with the solid solution to consequently form metal and Li_2O. However, Li_2O is primarily irreversible, but the presence of nanoscale α-MoO_3 nanoribbon leads to the reversibility of Li_2O, which has been reported earlier.[56, 57] From the CV cures shown in Fig 7 we can see that, two reduction peaks (0.253 and 0.421 V) associated with the insertion reaction appeared below 0.7 V and other two reduction peaks (1.261 and 1.404 V) appeared between 1 and 1.5 V, which shows Stage-I and stage-II took place simultaneously. Moreover, both the processes are reversible. The curves of the 6th cycle are almost identical to those of the 2nd cycle which show the MoO_3 @GNS anode is very stable and the de/intercalation of lithium is reversible which can explain the excellent cycling performance of α-MoO_3 nanoribbon@GNS essentially. The properties illustrated in Fig. 7 are consistent with those displayed in Fig. 6b.

It is surprising that we are not aware of such a good performance at these high rates in the literature. Especially, the performance at such high rates is much better than that of MoO_3 nanoparticles, [58] carbon-coated MoO_3, [18] MoO_3 nanowires and MoO_3 nanowire/Si coaxial-cable (ca. 780 mAh•g^{-1} at 100 mA•g^{-1}).[52] Based on the Table 1, it can be also seen that our sample shows greatly-enhanced high rate properties and stable cycling performance than those of MoO_3 nanoparticles, carbon coated MoO_3, MoO_3 nanowires and MoO_3 nanowire/Si coaxial cable. Our sample shows such excellent performances as anode materials for LIBs may result from its unique structure which can: 1) suppress the aggregation of α-MoO_3 nanoribbons, 2) accommodate the volume change during the cycle processes, 3) rise to a high α-MoO_3 in the composite (up to 93.1% by weight), 4) maintain a high electrical conductivity of the overall electrode (as shown in scheme 1).

Table 1 Comparison on electrochemical properties of modified MoO_3 as anode materials by different methods.

Sample[ref]	Methods	Current density（mA•g^{-1}）	Capacity（mAh•g^{-1}）（cycle number）	Cycle life
MoO_3@Carbon[18]	Hydrothermal	100	1064(50)	50
MoO_3 nanowire[52]	CVD	50	630 (20)	20
		100	590 (10)	10
MoO_3 nanowire @Si[52]	CVD	100	780 (15)	15
		200	580 (5)	5
MoO_3 nanoparticle[58]	Hydrothermal	400	600(150)	150
Presentwok[Fig6E,F]	Electrostatic Selfassembly	1000	754(200)	200
		1500	820 (30)	30
		3000	710 (30)	30

The EIS tests were applied to help us to further understand the reasons for the improved rate performances of the α-MoO_3@GNS anodes. Fig.8 shows the Nyquist plots of the MoO_3@GNS anodes and the pure MoO_3 nanoribbon anodes. Each Nyquist plot seemed to have a similar shape with a semicircle in the high-frequency region and a straight line in the low-frequency region. The semicircle in the high-frequency region can be associated with the charge-transfer process and the properties of electrochemical reaction resistance, which reflects the resistance for Li^+ ions migration through the electrolyte/electrode interface,[59] and the low frequency straight lines relate to the properties of the diffusion process. Inset of Fig. 8 shows the equivalent circuit model for the impedance spectra. R_s is the combination of electrolyte resistance and ohmic resistances of cell components. R_f and R_{ct} are represented for the film resistance and charge-transfer resistance, respectively. QPE1, QPE2, and Z_w are the capacitance of the surface-passivating layer, double layer capacitance, and the Warburg impedance, respectively. Fig. 8 shows the primary simulation parameters of α-MoO_3@GNS and pure MoO_3 nanoribbon anodes. As can be clearly seen in the chart, the R_{ct} (charge-transfer resistance) value of α-MoO_3@GNS (R_{ct}=230 Ω) is much smaller than that of pure MoO_3 nanoribbons (R_{ct}=400 Ω). This can be ascribed to the ultrathin nanoribbon structures of MoO_3 and perfect electronic conductivity of GNS, which could reduce the lithium-ion diffusion and electron transportation distance, and greatly enhance the ions transportation efficiency. This point is consistent with the structure characteristic of α-MoO_3@GNS illustrated in Figure 4C.

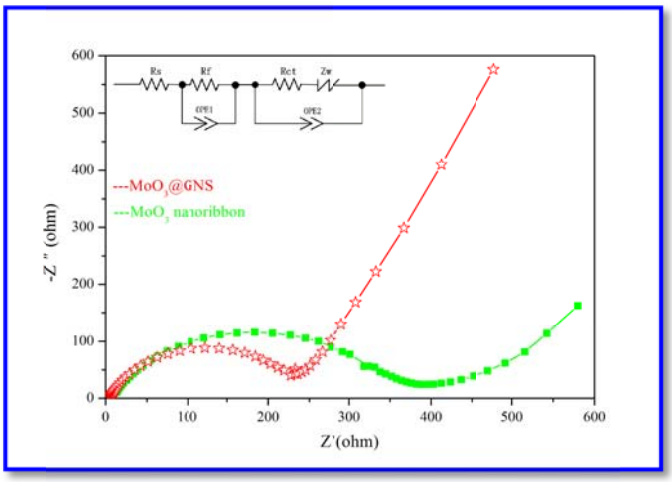

Fig. 8 Nyquist plots of nanoribbon α-MoO_3@GNS and pure MoO_3 nanoribbon.

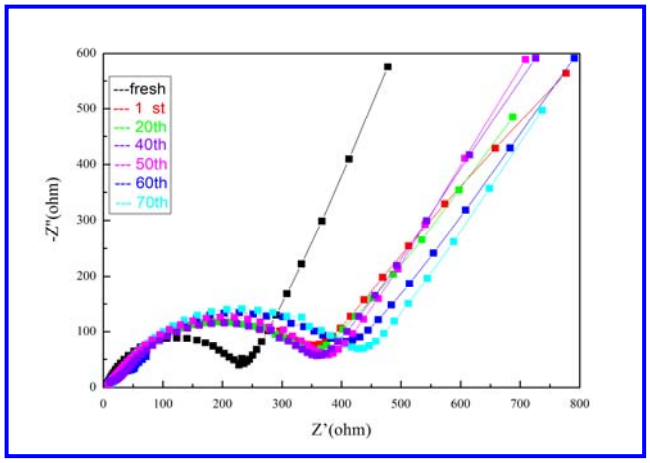

Fig. 9 Nyquist plots of nanoribbon α-MoO_3@GNS before cycling and after 1, 20, 40, 50, 60 and 70 galvanostatic charge/discharge cycles.

To further understand the electrode reaction kinetics of the nanocomposite, EIS measurements were carried out before cycling and after 1, 20, 40, 50, 60 and 70 galvanostatic charge/discharge cycles are carried out and the diffenrent Nyquist plots of the nanoribbon α-MoO_3@GNS electrodes are shown in Fig.9. It is seen that the charge-transfer resistance before cycling is lower than that in the 1st, 20th, 40th, 50th, 60th and 70th cycle. It is because the formation of SEI film when a current was applied. After 70 cycles, the charge-transfer resistance increases a little which is mainly because the continuous deposition of lithium ion in SEI film makes its thickness increase and then causes the increase of charge-transfer resistance, while the charge-transfer resistance only have a very little increase and nearly remain the same level which indicates the α-MoO_3@GNS has a perfect electron transport network and fast Li^+ diffusivity resulting from the incorporation of ultrathin GNS nanosheets and nanoscale α-MoO_3, and also illustrates the structure stability and perfect electron conductivity of α-MoO_3@GNS nanocomoposites.

5 Conclusions

A facile and effective way has been reported to synthesize α-MoO_3 nanoribbon@graphene nanosheeet nanocomposites through an electrostatic self-assembly method The characterizations of Raman, FT-IR, XRD, FESEM, TEM, SAED and HRTEM demonstrate that graphene nanosheets wrapped up the MoO_3 nanoribbon tightly and homogeneously and formed a robust composite structure. Compared to those structures of MoO_3 nanobelts grown on reduced graphene oxide or graphene, this unique hybrid architecture of graphene-encapsulated MoO_3 nanoribbon can take several advantages: 1) suppress the aggregation of α-MoO_3 nanoribbons, 2) accommodate the volume change during the cycle processes, 3) greatly improve the transportation efficiency of current carriers, 4) maintain a high electrical conductivity of the overall electrode. Most importantly, the α-MoO_3@GNS nanocomposites exhibits not only a high reversible capacitance (up to 823 mAh•g^{-1} after 70 cycles) but also an excellent cycling stability (with more than 754 mAh•g^{-1} after 200 cycles at 1000mA•g^{-1}) as well as a greatly-enhanced rate capability (displaying a high discharge capacity of 710 mAh•g^{-1} after 30 cycles at 3000mA•g^{-1}). We attributed the superior electrochemical performances of the α-MoO_3@GNS nanocomposites to their robust composite structure and the synergistic effect between MoO_3 nanoribbon and graphene nanosheet. EIS analysis confirms that the incorporation of graphene preserves the high conductivity and greatly enhances the transportation efficiency of Li^+ in the MoO_3@GNS nanocomposites during the electrochemical reaction. Therefore, the present results suggest that this kind of the α-MoO_3@GNS nanocomoposites hold a great potential as anode materials for high performance LIBs.

Acknowledgements

This work is partly supported by the National Natural Science Foundation of China (grant No. 51202297 and 61376018), Program for New Century Excellent Talents in University (NCET-12-0554), the National Basic Research Program of China (973 Program) grant No. 2013CB932901 and 2011 Program.

Notes and references

[a] School of Materials Science and Engineering, Central South University, Changsha, Hunan, 410083, China
[b] Key Laboratory of Nonferrous Metal Materials Science and Engineering, Ministry of Education, Central South University, Changsha 410083, Hunan, China
[c] State Key Laboratory of Information Photonics and Optical Communications, Beijing University of Posts and Telecommunications, Beijing 100876, China
*Corresponding author: liujun4982004@csu.edu.cn; Tel: (86)-0731-88836069; Fax: (86)-0731-88876692

1. W.-J. Li, S.-L. Chou, J.-Z. Wang, H.-K. Liu and S.-X. Dou, *Nano Letters*, 2013, **13**, 5480-5484.
2. M. Wu, J. E. C. Sabisch, X. Song, A. M. Minor, V. S. Battaglia and G. Liu, *Nano Letters*, 2013, **13**, 5397-5402.
3. J. M. Tarascon and M. Armand, *Nature*, 2001, **414**, 359-367.
4. B. Wang, X. Li, X. Zhang, B. Luo, Y. Zhang and L. Zhi, *Advanced Materials*, 2013, **25**, 3560-3565.
5. A. S. Arico, P. Bruce, B. Scrosati, J.-M. Tarascon and W. van Schalkwijk, *Nat Mater*, 2005, **4**, 366-377.
6. G.-W. Zhou, J. Wang, P. Gao, X. Yang, Y.-S. He, X.-Z. Liao, J. Yang and Z.-F. Ma, *Industrial & Engineering Chemistry Research*, 2012, **52**, 1197-1204.
7. Y. Gong, S. Yang, Z. Liu, L. Ma, R. Vajtai and P. M. Ajayan, *Advanced Materials*, 2013, **25**, 3979-3984.
8. X. Jia, Z. Chen, X. Cui, Y. Peng, X. Wang, G. Wang, F. Wei and Y. Lu, *ACS Nano*, 2012, **6**, 9911-9919.
9. Y.-S. Lin, J.-G. Duh and M.-H. Hung, *The Journal of Physical Chemistry C*, 2010, **114**, 13136-13141.
10. Z.-S. Wu, W. Ren, L. Wen, L. Gao, J. Zhao, Z. Chen, G. Zhou, F. Li and H.-M. Cheng, *ACS Nano*, 2010, **4**, 3187-3194.
11. H. Huang, W. Zhu, X. Tao, Y. Xia, Z. Yu, J. Fang, Y. Gan and W. Zhang, *ACS Applied Materials & Interfaces*, 2012, **4**, 5974-5980.

12. N. Yan, L. Hu, Y. Li, Y. Wang, H. Zhong, X. Hu, X. Kong and Q. Chen, *The Journal of Physical Chemistry C*, 2012, **116**, 7227-7235.
13. L. Shen, X. Zhang, H. Li, C. Yuan and G. Cao, *The Journal of Physical Chemistry Letters*, 2011, **2**, 3096-3101.
14. H. Su, T. Wang, S. Zhang, J. Song, C. Mao, H. Niu, B. Jin, J. Wu and Y. Tian, *Solid State Sciences*, 2012, **14**, 677-681.
15. T. M. McEvoy, K. J. Stevenson, J. T. Hupp and X. Dang, *Langmuir*, 2003, **19**, 4316-4326.
16. M. S. Whittingham, *Journal of The Electrochemical Society*, 1976, **123**, 315-320.
17. G. Zhao, N. Zhang and K. Sun, *Journal of Materials Chemistry A*, 2013, **1**, 221.
18. M. F. Hassan, Z. P. Guo, Z. Chen and H. K. Liu, *Journal of Power Sources*, 2010, **195**, 2372-2376.
19. H. Li, P. Balaya and J. Maier, *Journal of The Electrochemical Society*, 2004, **151**, A1878-A1885.
20. W. Pu, X. He, J. Ren, C. Wan and C. Jiang, *Electrochimica Acta*, 2005, **50**, 4140-4145.
21. H. G. Yang and H. C. Zeng, *Angewandte Chemie*, 2004, **116**, 6056-6059.
22. W. Dong and B. Dunn, *Journal of Non-Crystalline Solids*, 1998, **225**, 135-140.
23. R. Schöllhorn, R. Kuhlmann and J. O. Besenhard, *Materials Research Bulletin*, 1976, **11**, 83-90.
24. S.-H. Lee, Y.-H. Kim, R. Deshpande, P. A. Parilla, E. Whitney, D. T. Gillaspie, K. M. Jones, A. H. Mahan, S. Zhang and A. C. Dillon, *Advanced Materials*, 2008, **20**, 3627-3632.
25. J. S. Chen, Y. L. Cheah, S. Madhavi and X. W. Lou, *The Journal of Physical Chemistry C*, 2010, **114**, 8675-8678.
26. L. Zheng, Y. Xu, D. Jin and Y. Xie, *Journal of Materials Chemistry*, 2010, **20**, 7135-7143.
27. Y. Gu, F. Wu and Y. Wang, *Advanced Functional Materials*, 2013, **23**, 893-899.
28. J. Ji, H. Ji, L. L. Zhang, X. Zhao, X. Bai, X. Fan, F. Zhang and R. S. Ruoff, *Advanced Materials*, 2013, **25**, 4673-4677.
29. P. Kumta, 225th ECS Meeting (May 11-15, 2014), 2014.
30. S. J. R. Prabakar, Y.-H. Hwang, E.-G. Bae, S. Shim, D. Kim, M. S. Lah, K.-S. Sohn and M. Pyo, *Advanced Materials*, 2013, **25**, 3307-3312.
31. J. Yang, J. Wang, Y. Tang, D. Wang, B. Xiao, X. Li, R. Li, G. Liang, T.-K. Sham and X. Sun, *J. Mater. Chem. A*, 2013, **1**, 7306-7311.
32. M. Zhen, L. Su, Z. Yuan, L. Liu and Z. Zhou, *RSC Advances*, 2013, **3**, 13696.
33. H. J. Peng, J. Q. Huang, M. Q. Zhao, Q. Zhang, X. B. Cheng, X. Y. Liu, W. Z. Qian and F. Wei, *Advanced Functional Materials*, 2014.
34. J. Wang, J. Zhou, Y. Hu and T. Regier, *Energy & Environmental Science*, 2013, **6**, 926-934.
35. Y. Sun, J. Wang, B. Zhao, R. Cai, R. Ran and Z. Shao, *J. Mater. Chem. A*, 2013, **1**, 4736-4746.
36. Y. Dong, S. Li, H. Xu, M. Yan, X. Xu, X. Tian, Q. Liu and L. Mai, *Physical Chemistry Chemical Physics*, 2013, **15**, 17165-17170.
37. X. Yang, H. Ding, D. Zhang, X. Yan, C. Lu, J. Qin, R. Zhang, H. Tang and H. Song, *Crystal Research and Technology*, 2011, **46**, 1195-1201.
38. L. Noerochim, J.-Z. Wang, D. Wexler, Z. Chao and H.-K. Liu, *Journal of Power Sources*, 2012.
39. W. S. Hummers and R. E. Offeman, *Journal of the American Chemical Society*, 1958, **80**, 1339-1339.
40. Z.-S. Wu, W. Ren, L. Gao, B. Liu, C. Jiang and H.-M. Cheng, *Carbon*, 2009, **47**, 493-499.
41. K. S. Subrahmanyam, S. R. C. Vivekchand, A. Govindaraj and C. N. R. Rao, *Journal of Materials Chemistry*, 2008, **18**, 1517-1523.
42. L. Zhou, L. Yang, P. Yuan, J. Zou, Y. Wu and C. Yu, *The Journal of Physical Chemistry C*, 2010, **114**, 21868-21872.
43. J. Liu, S. Tang, Y. Lu, G. Cai, S. Liang, W. Wang and X. Chen, *Energy & Environmental Science*, 2013, **6**, 2691-2697.
44. Z.-S. Wu, W. Ren, L. Gao, B. Liu, C. Jiang and H.-M. Cheng, *Carbon*, 2009, **47**, 493-499.
45. S. Yang, X. Feng and K. Müllen, *Advanced Materials*, 2011, **23**, 3575-3579.
46. Z.-l. Wang, D. Xu, Y. Huang, Z. Wu, L.-m. Wang and X.-b. Zhang, *Chemical Communications*, 2012, **48**, 976-978.
47. Y. Shi, J.-Z. Wang, S.-L. Chou, D. Wexler, H.-J. Li, K. Ozawa, H.-K. Liu and Y.-P. Wu, *Nano letters*, 2013, **13**, 4715-4720.
48. M. Py, P. E. Schmid and J. Vallin, *Il Nuovo Cimento B Series 11*, 1977, **38**, 271-279.
49. M. Dieterle, G. Weinberg and G. Mestl, *Physical Chemistry Chemical Physics*, 2002, **4**, 812-821.
50. T. Tsumura and M. Inagaki, *Solid State Ionics*, 1997, **104**, 183-189.
51. Y. Iriyama, T. Abe, M. Inaba and Z. Ogumi, *Solid State Ionics*, 2000, **135**, 95-100.
52. P. Meduri, E. Clark, J. H. Kim, E. Dayalan, G. U. Sumanasekera and M. K. Sunkara, *Nano letters*, 2012, **12**, 1784-1788.
53. M. F. Hassan, Z. P. Guo, Z. Chen and H. K. Liu, *Journal of Power Sources*, 2010, **195**, 2372-2376.
54. P. Dickens and G. Reynolds, *Solid State Ionics*, 1981, **5**, 331-334.
55. A. Yu, N. Kumagai, Z. Liu and J. Y. Lee, *Journal of power sources*, 1998, **74**, 117-121.
56. P. Meduri, C. Pendyala, V. Kumar, G. U. Sumanasekera and M. K. Sunkara, *Nano letters*, 2009, **9**, 612-616.
57. P. Meduri, E. Clark, E. Dayalan, G. U. Sumanasekera and M. K. Sunkara, *Energy & Environmental Science*, 2011, **4**, 1695-1699.
58. S. H. Lee, Y. H. Kim, R. Deshpande, P. A. Parilla, E. Whitney, D. T. Gillaspie, K. M. Jones, A. Mahan, S. Zhang and A. C. Dillon, *Advanced Materials*, 2008, **20**, 3627-3632.
59. S. Yoon, C. Jo, S. Y. Noh, C. W. Lee, J. H. Song and J. Lee, *Physical chemistry chemical physics : PCCP*, 2011, **13**, 11060-11066.